Experimental and Numerical Investigation of a Non-Axisymmetric Strut Based Ejector

M. S. Balasubramanyam* **and D. Lineberry**
madhanb@uah.edu
Research Engineer, Propulsion Research Center
University of Alabama in Huntsville
Huntsville, AL 35899

C. P. Chen
Professor, Department of Chemical & Materials Engineering
University of Alabama in Huntsville
Huntsville, AL 35899

D. B. Landrum
Associate Professor, Department of Mechanical and Aerospace Engineering
University of Alabama in Huntsville
Huntsville, AL 35899

Abstract
Tests were performed in a non-axisymmetric, single nozzle, strut-based ejector to investigate mass flow entrainment, choking mechanisms and stream mixing as a function of primary (strut nozzle) to secondary (duct inlet) flow stagnation pressure ratio. Experimental results show a mass flow choke in the mixing duct rather than a traditional aerodynamic choke in the strut gap. The stream mixing length was constant for lower primary flow pressures, whereas mixing length varied with pressure at higher values. A companion numerical study was performed using Reynolds Averaged Navier-Stokes solutions to investigate several turbulence models. Based on both 2-D and 3-D simulation results, compressibility correction to conventional incompressible two-equation models was required for capturing the supersonic ejector mixing phenomena. The Baldwin-Lomax and the SST two-equation models were capable of capturing the essential flow features. Even with compressibility correction, the *k*-ε model could not reproduce wall-dominated phenomena such as mixing duct pressure recovery.

Keywords: *Combined Cycle Propulsion, Compressibility Effects, Numerical Validation*

NOMENCLATURE

A	Cross sectional area
k	Turbulent kinetic energy
M	Mach number
$\dot{m}_p$	Primary mass flow rate
$\dot{m}_s$	Secondary mass flow rate
P	Pressure
P_c	Chamber pressure
P_{os}	Secondary flow stagnation pressure
q	Heat flux

*Corresponding Author

R	Specific gas constant
T	Temperature
T_c	Chamber temperature
T_{os}	Secondary flow stagnation temperature

Greek Letters

ρ	Fluid density
ε	Dissipation rate
μ_t	Turbulent viscosity
γ	Ratio of specific heats
ω	Suction ratio

1. INTRODUCTION

Non-axisymmetric, ejector-based combined cycle propulsion (CCP) systems have received renewed attention due to their potential applicability to next generation space transportation systems [1]. The Strutjet is one of the RBCC systems under consideration [2]. This concept consists of a variable geometry duct with vertical engine struts mounted internally. Each strut has several rocket nozzles embedded within it. The engine operates in four modes: ducted rocket, ramjet, scramjet, and pure rocket. In the air-breathing modes, atmospheric air is ingested into the inlet and flows between the struts into the mixing section. The air is mixed with the fuel rich rocket exhaust and combusted. The combustion products are accelerated through an exit nozzle to provide the thrust.

A fundamental understanding of ejector physics is an enabling technology to realize an operational RBCC propulsion system. Supersonic ejectors perform the mixing and recompression of the primary flow (ejector) and the secondary (induced) flow [2]. The primary flow gets accelerated by a convergent divergent nozzle to reach supersonic velocity. By an entrainment-induced effect, the secondary stream is drawn into the flow and accelerated. Mixing and recompression of the resulting stream then occurs in a mixing chamber, where complex interactions take place between the mixing layer and shocks. Past theoretical and experimental ejector studies have considered one-dimensional, axisymmetric, or at best two-dimensional geometries. Concepts such as the Strutjet use a complex asymmetric, three-dimensional flow path. The objective of the current experimental effort was to characterize asymmetric ejector performance in terms of mass flow entrainment, stream mixing, and choking mechanisms. This study will help guide design of future RBCC systems and provide valuable data for validating computational fluid dynamic simulations of complex ejector systems.

Future RBCC engines will operate within a wide range of Mach numbers ($1 \leq M_\infty \leq 10.0$) and altitudes. The engine internal flows are highly turbulent and 3-Dimensional based on the geometrical configurations within the engine. The most common way to numerically account for turbulent effects is to use the Reynolds averaging approach (RANS). An important step in the validation process for Computational Fluid Dynamics (CFD) codes is to conduct numerical comparisons with experimentally investigated cases for which a detailed database is available. Validation of CFD models appropriate for supersonic through hypersonic flow applications requires careful consideration of the physical processes encountered at these flight regimes and detailed comparisons of the calculated results with experimental data sets that include these processes.

1.1 Experimental Ejector Facility

The UAHuntsville PRC cold flow ejector facility was originally designed to approximate the flow path of the Aerojet Strutjet concept [2, 3, 4]. The flow path consists of an approximately 8.9 cm by 10.2 cm rectangular cross section duct. An elliptically contoured converging inlet is located on the front end of the duct to provide uniform airflow from the laboratory. A single strut is installed in the duct approximately 63.5 cm downstream of the inlet. The single nozzle ejector strut is shown in Figure 1 .The strut has a rectangular cross section 2.5 cm wide by 17.8 cm tall. A rocket nozzle embedded in the strut provides the primary flow stream for the system. The approximately 2.1 cm by 2.1 cm nozzle has an area ratio of approximately 4.66 and transitions from a circular throat to a square exit.

Arrays of 48 static pressure taps are located along the centerlines of the top and side walls of the duct. The first two taps are spaced .64 cm apart followed by taps spaced 1.27 cm apart for 24.13 cm and 2.54 cm apart for 71.12 cm that follow. Ten static pressure taps are located on the centerline of the sidewall in the strut gap region of the duct. This region is located upstream of the rocket nozzle exit plane between the strut and the sidewall of the duct as shown in Figure 2. An aerodynamic fairing is located on the upstream end of the strut to provide uniform flow in the strut gap region. A Pitot-static probe is embedded in the strut fairing to measure the stagnation and static pressure of the secondary (induced) flow. A Pitot-static probe is also located in the center of the exit plane of the duct. This probe measures the stagnation and static pressures of the presumed fully mixed flow at the exit of the duct.

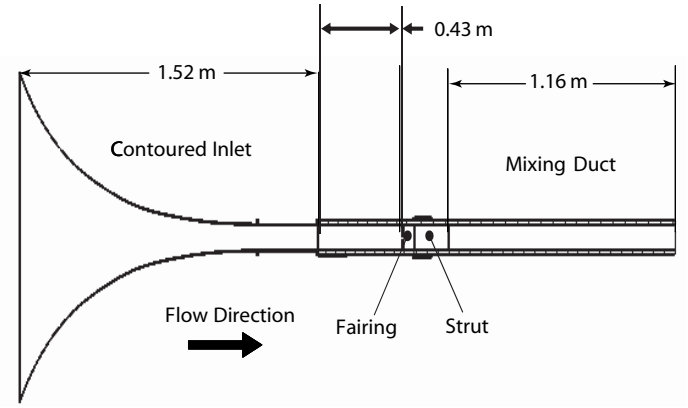

Figure 1. UAHuntsville PRC strut-ejector test rig configuration

An additional pressure tap is located in the rocket nozzle stagnation chamber to measure the stagnation or chamber pressure in the strut rocket chamber. The transducer connected to this pressure tap is connected to a feedback loop of a PID controller to maintain a relatively constant rocket chamber pressure for the experiment. In addition to the pressure instrumentation, two thermocouples mounted in the duct to measure chamber temperature and the secondary air stream temperature.

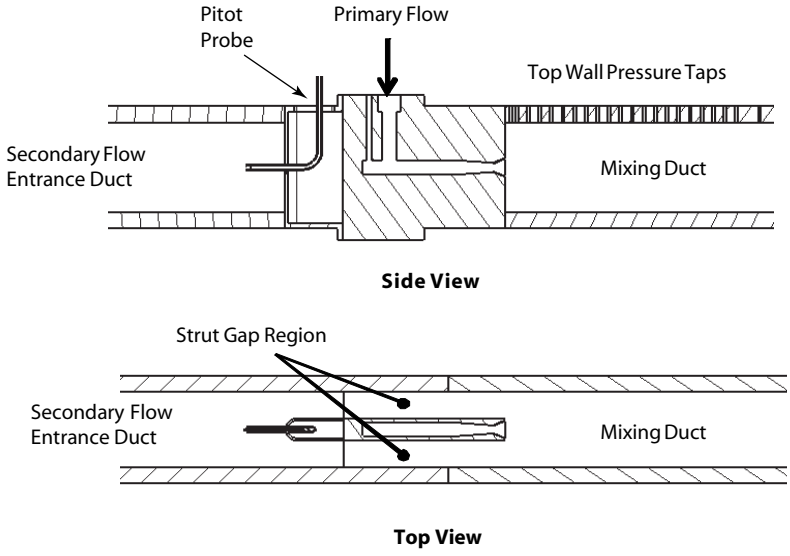

Figure 2. Strut-ejector flow path

1.1.1 Test Procedure

The detailed test series and procedure is described in Reference 5. Tests were conducted at nine different set points pressure ratios (P_c/P_{os}) from 6.5 to 60.5. Each set point was repeated ten times to provide an adequate statistical basis to assess repeatability and uncertainty. Tests were performed in steps of increasing chamber pressures and in steps of decreasing chamber pressures to assess any hysteresis effects. The results presented in this paper consist of accumulated data from nine tests on separate days. For calculated quantities (mass flow, mach numbers, suction ratio, etc.) the presented results are based on average values from these tests. Appropriate uncertainty estimates were determined following the approach outlined in Coleman and Steele [6], to account for both the variation of the measured quantities and of the variation in the set point between tests.

1.2 Numerical Modeling Approach

The equations governing the ejector flow field are the compressible Favre-averaged Navier-Stokes equation for the conservation of mass [7]. The mass conservation equation is given by

$$\frac{\partial \rho}{\partial t} + \frac{\partial}{\partial x_j}(\rho u_j) = 0 \tag{1}$$

where ρ is the Reynolds-averaged mixture density and u_j is the mass averaged velocity in the j^{th} direction. The conservation of momentum equations in summation notation are

$$\frac{\partial}{\partial t}(\rho u_i) + \frac{\partial}{\partial x_j}(\rho u_i u_j) = \frac{\partial}{\partial x_j}[-(p + \frac{2}{3}\rho k)\delta_{ij} + \tau_{ij}] \tag{2}$$

In equation 2, the stress term is modeled as

$$\tau_{ij} = \left(\mu + \mu_t\right)\left(\frac{\partial u_i}{\partial x_j} + \frac{\partial u_j}{\partial x_i}\right) - \frac{2}{3}\left(\rho k + \mu_t \frac{\partial u_i}{\partial x_i}\right)\delta_{ij} \tag{3}$$

where p is the pressure, k is the turbulent kinetic energy, δ_{ij} is the Kronecker delta and τ_{ij} is the shear stress tensor. The conservation of total energy per volume is

$$\frac{\partial}{\partial x_j}[(E_t + p)u_j] + \frac{\partial q_j}{\partial x_j} + \frac{\partial}{\partial x_i}(u_j \tau_{ij}) - \frac{\partial}{\partial x_j}(\sum_{s=1}^{ns} h_s J_{s,j}) \tag{4}$$

where is E_t is the total energy per volume, q_j is the heat flux in the j^{th} direction and the far right summation term is the effect of heat transfer due to species molecular diffusion.

1.2.1 Turbulence Models

The turbulence models are based on Favre (mass-weighted) averaging the equations governing the flow. Favre averaging introduces additional terms known as Reynolds stresses. These stresses are modeled using the Boussinesq eddy viscosity concept [8]. The eddy viscosity is a property of the flow, not a physical property of the fluid. Following the kinetic theory of gases, the eddy viscosity is generally modeled as the product of a velocity scale q and a length scale l, $\mu_t \approx \bar{\rho} q l$. The turbulence models differ in the way q and l are estimated. Eddy viscosity models are typically categorized by the number of additional transport equations to be solved. The models available are zero, one, and two equation models. Zero equations use algebraic formulae to relate the velocity and length scales to local mean flow conditions. In this current numerical investigation the algebraic turbulence Baldwin-Lomax model [9], the Spalart Allmaras Model [10], the Standard k-ε Model [11] and the Menter's Shear Stress Transport (SST) Model [12] were used for the comparative comparisons.

1.2.2 Numerical Algorithm

The governing equations are solved using the ESI Corporation's CFD-FASTRAN code [7]. The density-based flow solver is applicable from low sub-sonic (Mach = 0.1) to hypersonic speeds. The flux vector and flux Jacobians are evaluated based on the upwind schemes for the convective (convective-moving) fluxes. Roe's approximate Riemann solver [14] is used for the flux difference scheme. The

Osher-Charkravarty [15] flux limiter was used for these computations. The solution for the discretized equation is achieved by a time marching algorithm. For steady flows, the time marching scheme is repeated until residuals or the change in the solution variables fall below a tolerance level or reach machine zero. The time marching scheme produces a time-accurate answer for a transient or unsteady simulation. An implicit time marching scheme was adopted for this evaluation. The implicit schemes are a block diagonal iterative method (point implicit in the GUI) and a Jacobi-point iterative (fully implicit in the GUI) method.

2. EXPERIMENTAL RESULTS

2.1 Mass Flow Augmentation

For RBCC applications, the secondary flow mass entrainment is a critical aspect of the air breathing portions of flight. For the current experimental apparatus, secondary mass flow was calculated from the stagnation and static pressures measured by a Pitot-static probe upstream of the strut, and from the inlet temperature of the flow. The mass flow was calculated according to

$$\dot{m}_s = \sqrt{\frac{\gamma}{R}}\frac{P_s}{\sqrt{T_{os}}}A\sqrt{\left(\frac{P_{os}}{P_s}\right)^{\frac{\gamma-1}{\gamma}}\frac{2}{\gamma-1}\left(\left(\frac{P_{os}}{P_s}\right)^{\frac{\gamma-1}{\gamma}}-1\right)}, \quad (5)$$

where γ was taken as 1.4 and R is taken as 287 J/kgK. The cross-sectional area of the duct is reduced from the geometric area to account for boundary layer effects. A simple flat plate approximation using a displacement thickness calculated from the Reynolds number of the centerline flow was used to estimate the area reduction. The mass flow of the primary stream was calculated based on the assumption that the flow is choked at the throat of the rocket nozzle using the equation

$$\dot{m}_p = \frac{P_c}{\sqrt{T_c}}A\sqrt{\frac{\gamma}{R}\left(\frac{2}{\gamma+1}\right)^{\frac{\gamma+1}{\gamma-1}}}, \quad (6)$$

where γ and R have the same values as (10) but the A is the nozzle throat area. The ratio of the primary to secondary mass flow rates is called the suction ratio (ω). This quantity is the amount of secondary flow that can be induced for a given primary mass flow. Figure 3 shows the primary and secondary mass flow rates along with the suction ratio plotted against the pressure ratio.

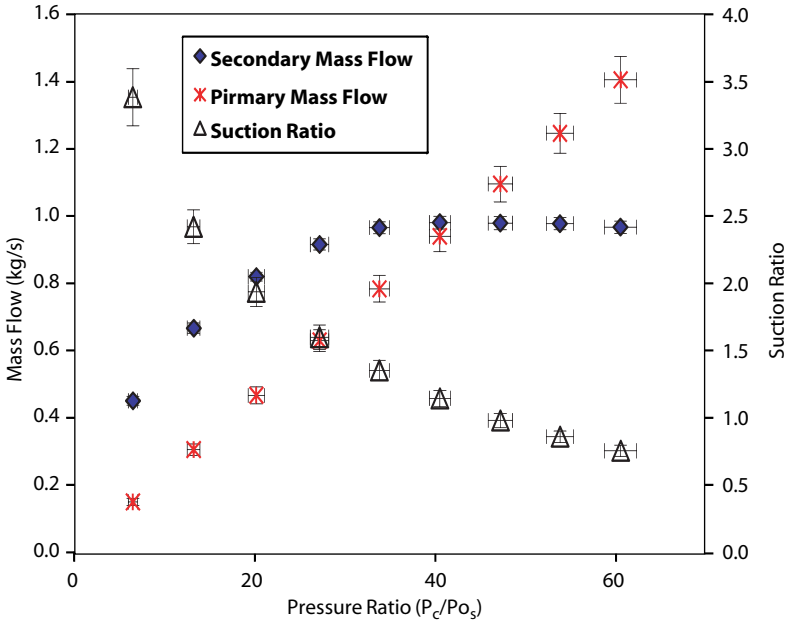

Figure 3. Primary and secondary mass flow comparison.

As can be seen in Figure 3, the secondary mass flow becomes approximately constant at 0.96 kg/s around a pressure ratio of 34. This corresponds to a primary mass flow of about 0.78 kg/s. The primary mass flow, which is a function of the chamber pressure, increases steadily with increasing chamber pressure. The leveling-off of the secondary mass flow trace is indication that the flow has become choked and that the mass flow can only be increased at this point by changing the stagnation conditions of the secondary flow. To examine the choking mechanism, the pressure ratios in the strut gap were examined. Figure 4 shows the ratio of the static wall pressure to the total pressure of the secondary flow at the final strut gap position.

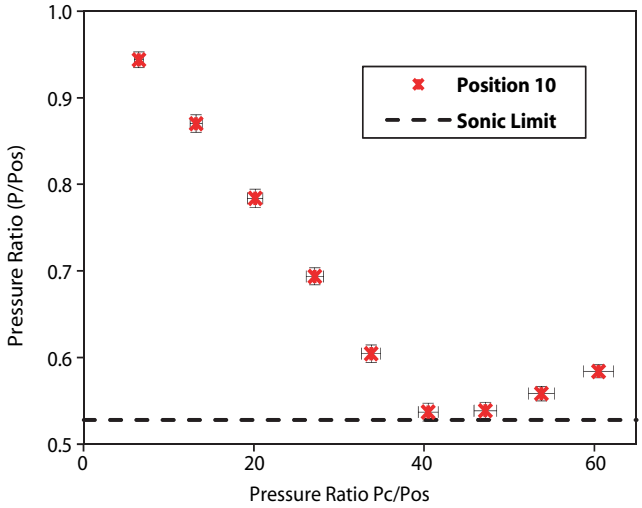

Figure 4. Strut gap Position 10 Pressure Ratio

From Figure 4, it can be observed that as the set point pressure ratio increases the pressure ratio in the strut gap approaches the sonic limit for air (0.528). At a set point pressure ratio of 40, the pressure ratio in the strut gap reaches the sonic limit indicating that the choking mechanism for the secondary flow is a traditional aerodynamic choke. As the set point increases above 40 the pressure ratio increases (away from the sonic limit). At these higher set points the choking mechanism for the secondary flow is not a traditional aerodynamic choke. The flow remains choked as indicated by Figure 3. Thus at these higher set points a Fabri mass choke of the secondary flow occurs [16, 17].

The Mach number of the secondary flow upstream of the strut and the presumed mixed flow at the exit of the duct were evaluated. Total and static pressures were measured upstream of the strut for the secondary flow and in the center of the duct exit for the mixed flow. The resultant Mach numbers were determined from the ratios of the measured total and static pressures. For subsonic flow the Mach number was calculated according to

$$M_s = \sqrt{\frac{2}{\gamma - 1}\left(\left(\frac{P_{os}}{P_s}\right)^{\frac{\gamma-1}{\gamma}} - 1\right)}, \tag{7}$$

where Po_s is the measured stagnation pressure, P_s is the local static pressure , and γ is the ratio of specific heats (equal to 1.4 for air). At the duct exit the flow could be subsonic or supersonic. To account for a shock induced by the probe in the supersonic flow, the Mach number was calculated according to

$$\frac{P_o}{P_1} = \left[1 + \frac{2\gamma}{\gamma+1}\left(M_1^2 - 1\right)\right] \cdot \left[1 + \frac{\gamma-1}{2}\left(\frac{1 + \frac{\gamma-1}{2}M_1^2}{\gamma \times M_1^2 - \frac{\gamma-1}{2}}\right)\right]^{\frac{\gamma}{\gamma-1}}, \tag{8}$$

where P_o is the stagnation pressure measured by the probe, P_1 is the static pressure upstream of the flow upstream of the probe, and γ is the ratio of specific heats. The appropriate equation for the exit Mach number depends on the ratio of the stagnation pressure to the side wall static pressure at the exit. If this ratio is less than 1.89, then the flow is subsonic, and Eq. 12 is used. If the pressure ratio is greater than 1.89, then the flow will be sonic, a shock will form in front of the probe, and Eq. 13 must be used.

Figure 5 shows the Mach numbers of the secondary flow at the fairing and of the mixed flow at the duct exit at each chamber pressure. The secondary flow Mach number reached a constant value of approximately 0.28 at a set point of approximately 34. This is consistent with the secondary mass flow choking indicated in Figures 3 and 4. The Mach number at the duct exit increased to a value of approximately 0.625 where it began to level-off around a chamber pressure of 35 psi. As chamber pressure was increased above 40, the exit Mach number began to increase again and became sonic around a set point of 53.7. Mixing duct exit pressure profiles indicated that at these higher set points the secondary flow was not fully mixed with the supersonic core of the primary jet.

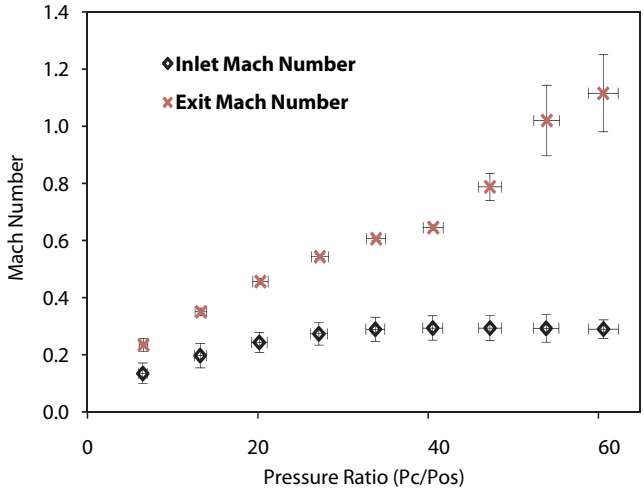

Figure 5. Inlet and Exit Mach Numbers

2.2 Mixing Section Static Pressures

Static pressure measurements along the centerlines of the top and side walls of the duct downstream of the strut exit plane were used to evaluate mixing of the primary and secondary flow streams. Figure 6 shows a plot of the normalized pressures for set points of 20.2, 40.5, and 53.8. The pressures in the figure have been normalized by dividing by the secondary flow total pressure at the inlet (the lab atmospheric pressure). The first two sets of data show the low pressure trend. For these data the pressure at the first sidewall position is equal to the last strut gap pressure. The pressure then begins to recover gradually until it reaches a pressure equal to the duct back pressure by an axial location (L/d_h) of approximately 21. The top wall data indicate a recirculation region immediately downstream of the strut. The first two pressure taps have values equal to the secondary flow stagnation pressure. At the third pressure tap the top wall pressures dropped to values almost equal to the sidewall pressures. The top wall pressure recovers gradually, in a manner similar to the sidewall pressure until an axial location of approximately 21. This pattern was visible in all tests with pressure ratios below 50.

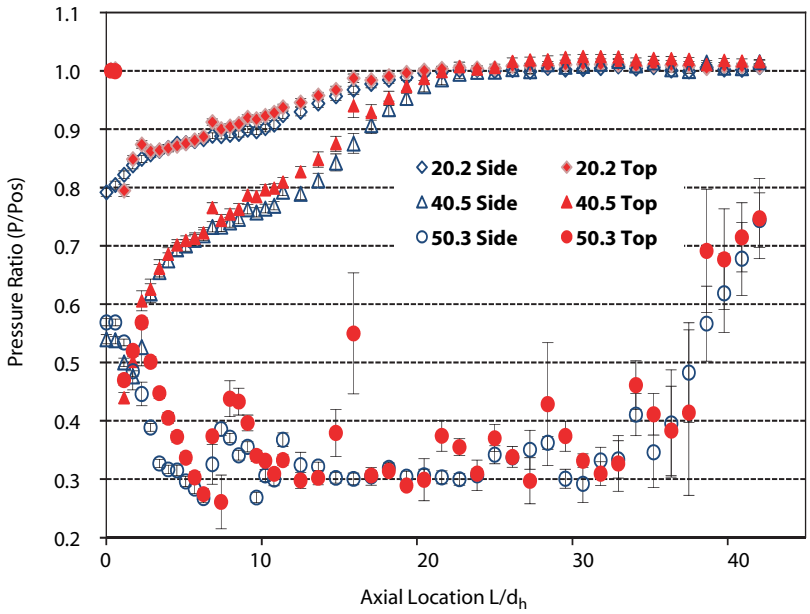

Figure 6. Top and side wall pressure distributions for three set point pressure ratios.

The third set of data on Figure 6 shows the high pressure trend. The pressure ratio set point for this test was 50.3. The data for the top wall pressures indicate the same recirculation region immediately downstream of the strut. Both the top and sidewall pressures show a decrease in pressure to a pressure ratio of approximately 0.27 at an axial location (L/d_h) of 8. The pressures show a region of approximately steady pressure around a pressure ratio of 0.3 for L/d_h between 8 and 20. Within this region there appears to be shock structure which impinges on the wall. These shocks were verified with Schlieren imaging. At approximately $L/d_h = 35$ the pressures begin to recover. For this test the pressure does not fully recover to the back pressure (pressure ratio of 1) by the end of the instrumented duct. This high pressure trend was present for all tests with operating pressure ratios above 50, however length of the steady region at 0.3 psi varied directly with the set point pressure ratio.

3. NUMERICAL RESULTS

As described in Lineberry et al., [4] the 3-D non-axisymmetric ejector flow system involves complicated phenomena including shock-boundary layer interaction, mass choking, jet mixing and secondary flow separations. To systematically study these flow features, the first step was to select an appropriate turbulence model for the RANS calculations. Specifically, we are most interested in the ejector mass choking phenomena created by a high-pressure jet within confined environments, as well as the mixing patterns. Due to the high aspect ratio geometry of the single-strut configuration, it was beneficial to carry out detailed 2-D simulations to first investigate the relative performance of the various turbulence models. The sidewall database was chosen for this purpose. The ejector geometry used in the computational simulations is depicted in Figure 1. The primary stream is accelerated through a convergent-divergent nozzle to a supersonic Mach number ($\approx$ 3.0). The secondary stream flows through the strut gap and is then entrained by the primary flow. The flow in the duct downstream of the ejector experiences a series of normal and/or oblique shock waves [18, 19]. Farther downstream these shocks stabilize and disappear. The primary flow may maintain a supersonic core or become subsonic depending on the chamber pressure of the rocket.

A 2-D multi-block computational grid system was used for the initial numerical studies. The grids used in the calculations were structure grids in each zone with exponential stretching functions. A non-dimensional wall distance, y^+, of about 30 was set for the k-ε model utilizing wall-functions, and about

1 for the other models. Grid refinement studies were conducted until a grid independent solution was achieved. The number of cells used in the 2-D computational grid was 19,152.

3.1 Numerical Computations

The upstream boundary conditions at the secondary flow inlet were evaluated utilizing the compressible flow relationships for given total pressure (P_0) and Temperature (T_0) conditions and assuming Mach 0.2 flow. The primary flow (rocket) exit boundary conditions were obtained by separately modeling the 3-D nozzle flow field. As an example, Figures 7a and 7b show the detailed Mach number and pressure profiles at the exit planes of the nozzle for the 600 psi chamber pressure case.

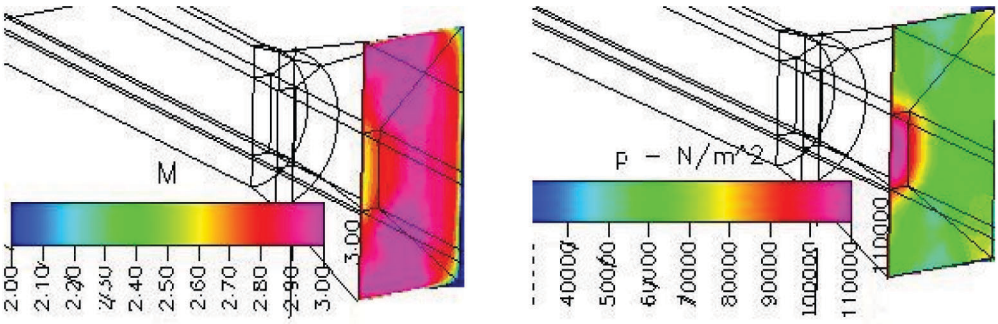

(a) (b)

Figure 7. 3D Strut rocket nozzle exit (a) Mach contours; (b) Pressure contours

The volume-averaged values were then calculated and uniformly imposed at the exit plane of the 2-D nozzle to start the calculation. To further justify the 2-D approach taken in this study, normalized sidewall pressure profiles versus the normalized length in the mixing region, predicted using the Baldwin-Lomax model from both 2-D and 3-D calculations are compared to side-wall data as shown in Figure 8. The comparison is qualitatively satisfactory. The discrepancy between the two numerical results is due to grid resolution in the 3-D case as well the difference in the rocket nozzle exit conditions. In the 3-D calculation, the inlet condition for the primary flow was specified and thus boundary layer development at the nozzle exit plane was accounted for.

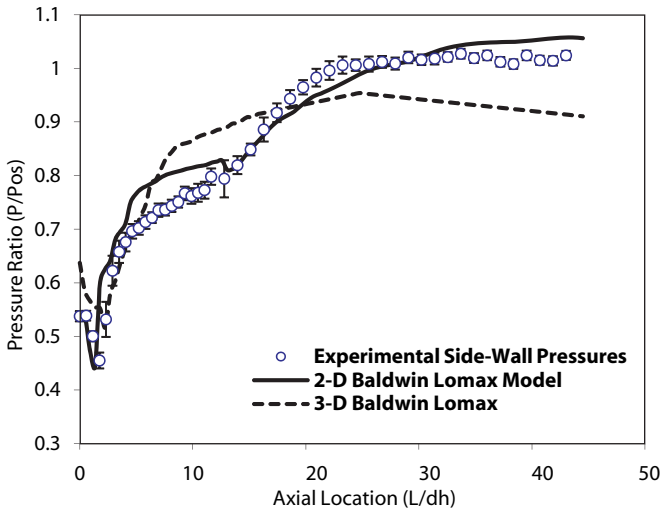

Figure 8. Comparative 2D/3D downstream sidewall normalized pressure profiles for ejector chamber pressure of 600 psi

In the 2-D simulations, the calculation started at the nozzle exit plane and the thermal fluids conditions were taken to be uniform. The exact boundary conditions at the ejector duct exit plane were found to be very sensitive to the flow calculations within the mixing region. To fully resolve this issue, very fine grid resolution is required for the full 3-D calculation and these studies are scope for future studies. For the purpose of turbulence model selection, detailed grid-resolved 2-D calculations are sufficient. The boundary conditions for the top walls are adiabatic walls with no slip conditions. Extrapolated boundary conditions were applied at the mixing duct exit, i.e., this outlet subtype extrapolates all boundary information from the cell center to the boundary face if the Mach number at the cell center is greater than 1.0. The simulations were marched in pseudo-time until a steady state was reached. A steady state was assumed when all variable residuals (mass, momentum, energy and turbulence transport) were reduced from their initial values by at least four orders of magnitude. For steady state problems, the convergence is further sped up by a local time stepping procedure in which a constant CFL number is used in all the control volumes. The simulation was run for 3000 cycles to ensure that all measurement variables achieved steady state. Convergence was determined when the solution no longer changed.

The flow field calculations within the strut gap region were first examined computationally. This is important because accurate secondary flow profiles at the strut exit plane set up correct boundary conditions for the mixing section fluid dynamics. In a confined ejector system as shown in Figure 2, an aerodynamic choke may occur at a minimum geometric area. The choked, sonic limit is assumed to be reached in the air secondary flow when the local static pressure is equal to a factor of 0.528 of the secondary stagnation pressure. For a 1 atm (101325 Pa) inflow, this corresponds to a local static pressure of approximately 53,500 Pa. This behavior was experimentally observed in the strut gap region. For ejector chamber pressures up to 600 psi the strut gap pressures were observed to steadily decrease toward the sonic limit as seen in Figure 9.

As the rocket chamber pressure was increased above 600 psi the local static pressures in the strut gap remained above this the sonic limit. Considering the secondary mass flow rate appears to choke at a primary pressure between 500 to 600 psi, this movement away from the sonic limit suggests that the flow does not choke in the strut gap at pressures higher than 600 psi. The numerical predictions for the strut gap flow, shown in Figures 9 and 10, generally correlate with the experimental observations.

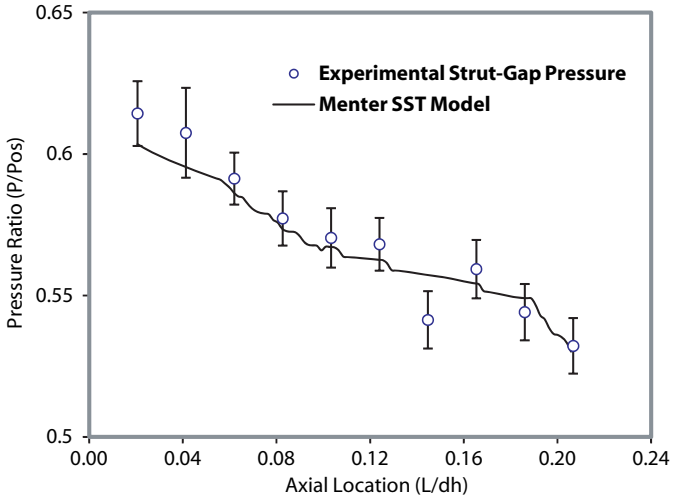

Figure 9. Normalized ejector strut gap sidewall pressure profiles for ejector chamber pressure 600 psi

Comparing the normalized sidewall pressure profiles for the 600 psi case (Figure 9), the static pressure at the end of the strut gap is just at the sonic limit. For the 800 psi chamber pressure case (Figure 10), it can be seen that the pressure level increases away from the sonic limit. Although there are a few local discrepancies, the numerical results compare reasonably well with the experimental data.

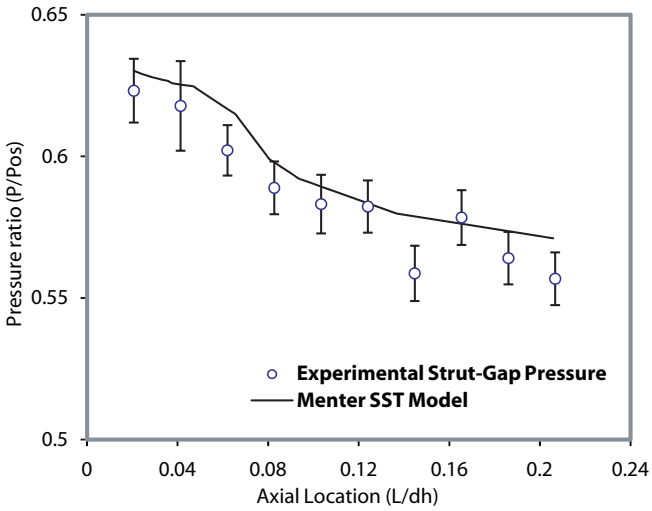

Figure 10. Normalized ejector strut gap sidewall pressure profiles for ejector chamber pressure of 800 psi

Next the flow field in the mixing section just downstream of strut exit plane and ejector exit plane was investigated. Experimental data pertaining to three sets of rocket chamber pressures, 300, 600 and 800 psi, were used to validate the turbulence models used in the numerical calculations. As the chamber pressure changes from low (300 psi) to higher pressures (600 and 800 psi), the sidewall pressure profile pattern changes drastically. At a chamber pressure of 600 psi (Figure 11), the sidewall pressure decrease after passing the strut exit plane then begins to recover.

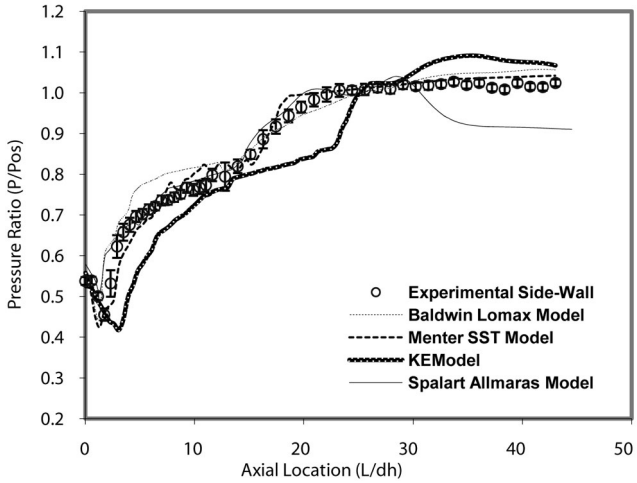

Figure 11. Normalized sidewall pressures in ejector mixing duct for ejector chamber pressure of 600 psi

Relative performance of the turbulence models are plotted for this case as this adverse pressure gradient represents a severe test case for turbulence modeling. Comparative results from Figure 11 indicate that the performance of the Menter-SST and the Baldwin-Lomax models were superior to those of the Spalart-Allmaras and the *k*-ε models. The one equation Spalart-Allmaras model shows a rapid pressure recovery indicating excessive mixing. On the other hand, the *k*-ε model is not capable of handling the adverse pressure gradient due to its use of wall-functions. The complete mixing of the primary and secondary streams is indicated when the sidewall pressures recover to the atmospheric pressure.

At lower chamber pressure, i.e. 300 psi, Figure 12 shows sidewall pressures immediately recovers from the strut gap exit plan and reach atmospheric very quickly. Experimental observations indicated that this occurred at about 0.4 m downstream of the ejector. Comparisons between experimental data and numerically computed values indicate that the Menter-SST turbulence model predicts this mixing region more accurately than the Baldwin Lomax model. As mentioned above, the mixing duct pressure profiles change character for primary chamber pressures above 600 psi. The sidewall pressure ratio decreases after passing the strut exit plane and recovers. The mixing length for the 600 psi chamber pressure was found to occur experimentally at about 0.88 m. Comparisons of data and numerically predicted values shown in Figure 11 indicate that the Menter-SST turbulence model more accurately predicts the mixing length than the Baldwin Lomax model, which under predicts the mixing length. For ejector chamber pressure of 800 psi (Figure 13) the sidewall pressure never fully recovers, indicating poor mixing in the duct. This behavior has also been established by total pressure traverses in the duct exit plane that show a supersonic primary flow core remains for high rocket chamber pressures. The pressure discontinuities at these high chamber pressures indicate the presence of shock waves in the flow field. Comparisons of data with numerically computed pressures indicate the Menter-SST model predicts the mixing length better than the other turbulence models. However, the Baldwin-Lomax model performs better in capturing the shock wave regions.

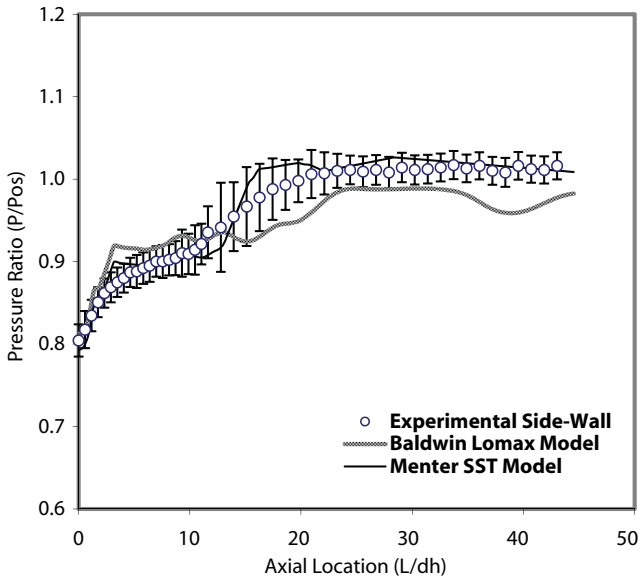

Figure 12. Normalized side-wall pressures in ejector mixing duct for ejector chamber pressure of 300 psi

Compressibility effects, which reduce mixing and turbulent intensity are present in supersonic free shear aero-propulsive flows and can be significant for large convective Mach numbers. A parameter that could be used to characterize the effect of compressibility on the turbulent fluctuations is the turbulent Mach number, which is defined as the ratio of a characteristic speed of turbulence to the wave speed. Thus $M_t = \sqrt{2}k/a$, where 'k' is the turbulent kinetic energy and 'a' is the speed of sound. As

pointed by various researchers [20, 21] the standard *k*-ε model fails to predict the observed decrease in spreading rate for the compressible free shear layers. Compressibility is modeled using dilatational and pressure fluctuation terms within the turbulence quantity conservation equations. Concentrating on the *k*-ε model, the dissipation of the kinetic energy in compressible turbulence was argued to be augmented by the dilatational components ε_d of the dissipation tensor in addition to the solenoidal components. Sarkar et al. [22], considered the evolution of the turbulence fluctuations on an acoustic time scale.

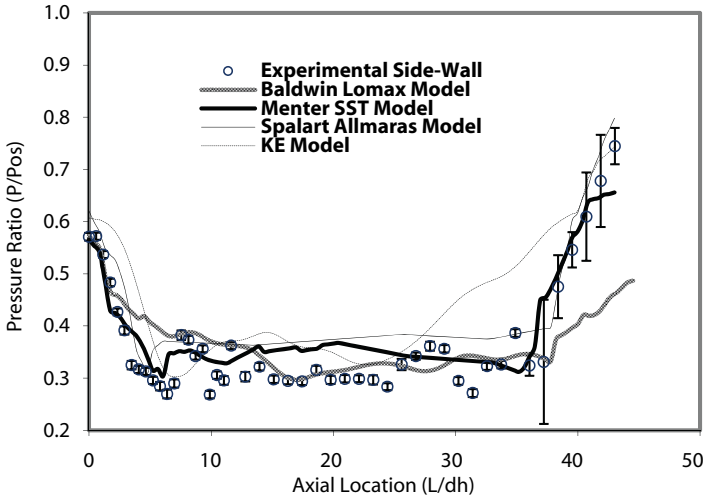

Figure 13. Normalized sidewall pressures in ejector mixing duct for ejector chamber pressure of 800 psi

They considered the effect of varying compressibility based on the turbulent Mach number M_t, on the rate of dissipation of turbulent kinetic energy, ε. Analysis of decaying compressible turbulence on the solenoidal component of the dissipation rate was negligible in comparison with the effect on the dilatational component, ε_d. They also observed that the ratio of dilatational dissipation rate to the solenoidal dissipation rate varied directly as the square of the turbulent Mach number M_t. They proposed a model for the dilatational dissipation rate, which is given as, $\varepsilon_d = \alpha_1\, \varepsilon\, M_t^2$, where α_1 is an arbitrary constant of order 1. Adding the above term would account for the compressibility correction in the conventional two-equation model. The baseline two-equation model used in this study is the standard *k*-ε model, written for mass weighted turbulence quantity for turbulence kinetic energy '*k*' with the extra compressibility term being:

$$\frac{\partial}{\partial t}(\rho k) + \frac{\partial}{\partial x_j}(\rho u_j k) = P - \rho\varepsilon + \frac{\partial}{\partial x_j}\left[\left(\mu + \frac{\mu_t}{\sigma_k}\right)\frac{\partial k}{\partial x_j}\right] - \alpha_1 \frac{k}{a^2}\rho\varepsilon \tag{9}$$

where $\alpha_1 = 2.0$, and its dissipation rate 'ε' are

$$\frac{\partial}{\partial t}(\rho\varepsilon) + \frac{\partial}{\partial x_j}(\rho u_j \varepsilon) = C_{\varepsilon_1}\frac{P\varepsilon}{k} - C_{\varepsilon_2}\frac{\rho\varepsilon^2}{k} + \frac{\partial}{\partial x_j}\left[\left(\mu + \frac{\mu_t}{\sigma_k}\right)\frac{\partial \varepsilon}{\partial x_j}\right] \tag{10}$$

Sarkar et al. [22] and Zeman [20] have postulated that the transport equation for ε is unaffected by compressibility. The compressibility corrections were incorporated into the density-based CFD-FASTRAN® code [7], for the *k*-ε turbulence model. Figures 14 and 15 show the comparison of calculated side-wall pressures with the experimental data for strutjet chamber pressures of 600 and 800 psi. The *k*-ε model with and without compressibility corrections, and the SST model were used in these CFD calculations.

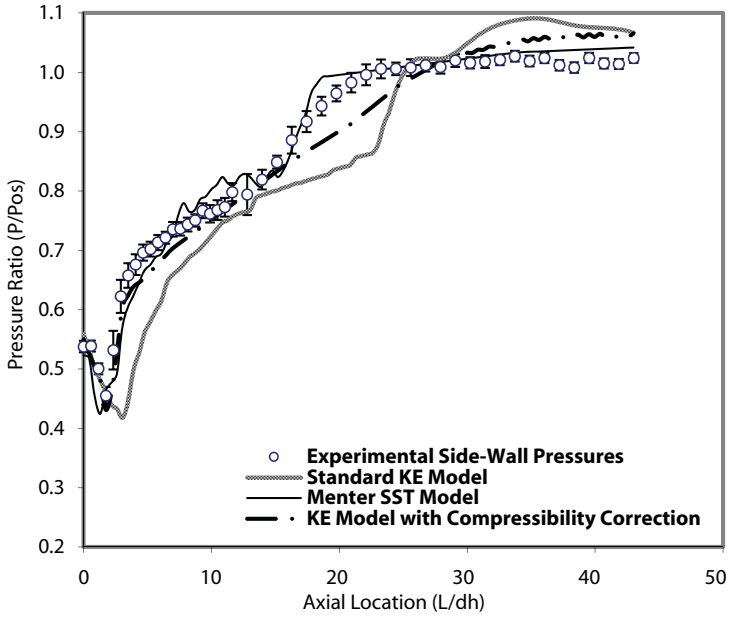

Figure 14. Normalized side-wall pressure comparisons for ejector chamber pressure at 600 psi

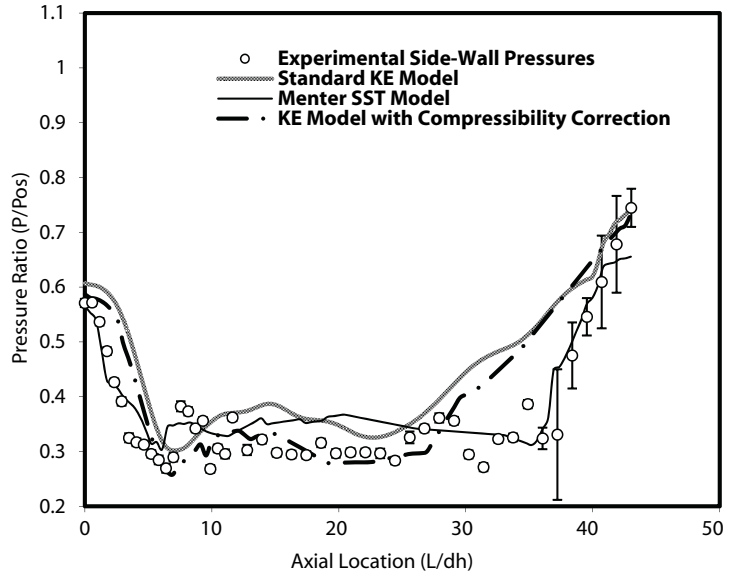

Figure 15. Normalized side-wall pressure comparisons for ejector chamber pressure at 800 psi

As pressure level of the ejector changes, the flow pattern changes drastically. At a chamber pressure of 600 psi, the mixing length was about 0.88 m, from experimental data. The complete mixing of the primary and secondary streams is indicated when the side wall pressures recover to the external condition, i.e. 1 ATM. From these figures, it can be seen that within the mixing zone, the compressibility corrected k-ε model shows much improved predictions when compared with the standard k-ε model and experimental data. However, after the complete mixing zone, the wall effect becomes dominant, and the wall function approach used in both k-ε models (with and without compressibility correction) cannot capture the pressure recovery. On the other hand, the SST model performs well in the recovery regions due to its use of k-ω formulation at the wall region as seen clearly in Figs. 14 and 15.

3.3 Three Dimensional Flow Characteristics

One flow characteristic associated with the non-axisymmetric ejector flow field is the three-dimensionality in the strut-base region. As depicted in Figure 16, as the primary stream is accelerated through a convergent-divergent nozzle to a supersonic Mach 3 jet, the secondary stream flows through the strut gap and is then entrained by the primary flow. When the secondary flow tries to expand around the corner as it passes the strut, a separation region will be formed, characterized by low static pressures. The experimental study of Reference 17 also supplied pressure distribution data at the top wall. A full 3-D CFD calculation was required to capture this flow feature.

As seen in Figure 17, the compressibility-corrected k-ε model improves predictions within the mixing zone, similar to the 2-D results. However, the good agreement between the prediction and data in the strut base region and the ability of capturing the flow separation by both the Baldwin-Lomax model and the SST model indicated that turbulence models capable of resolving near wall regions should be used for this 3-D ejector flow field. Both the SST model and the Baldwin-Lomax model did not capture the correct spreading of the mixing layer within the mixing zone. Compressibility correction to the SST model, similar to the approach taken by Forsythe et al. [23], should be further investigated.

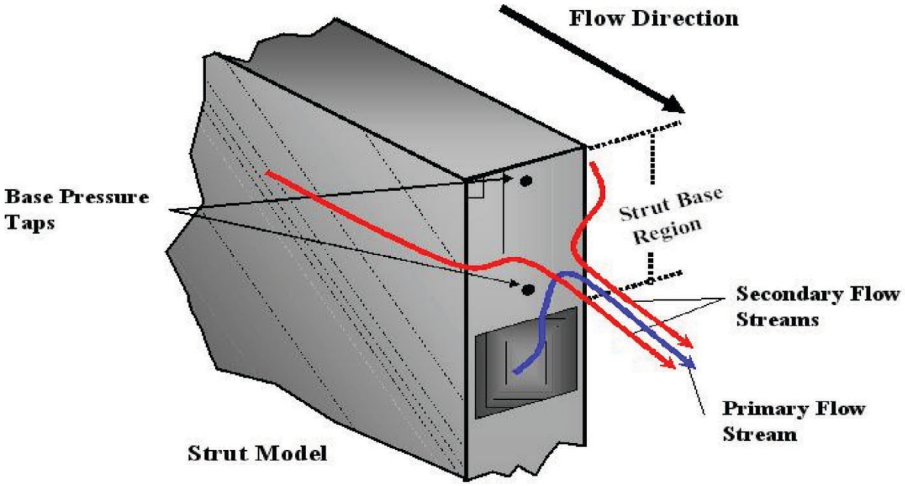

Figure 16. Strut-base separation region

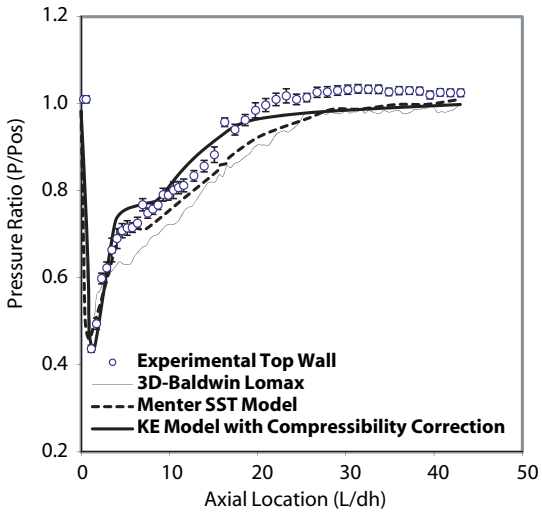

Figure17. 3-D Pressure profiles at centerline of top-wall for ejector chamber pressure 600PSI

Discussion

Conducting the ejector tests at various primary (nozzle) to secondary (duct inlet) total pressure ratios (set points) between 6.5 to 60.5 provided the opportunity to evaluate secondary flow choking mechanisms, mass flow entrainment and duct mixing length. Secondary total pressure remained constant since the induced flow was entrained from ambient laboratory conditions. A choke of the secondary mass flow was first observed at pressure ratio of 40.5 and higher, which correspond to a primary mass flow of 2 lbm/sec. The secondary flow remained choked as primary pressure increased. From the examination of measured strut gap and duct wall static pressure profiles, it was concluded that this was a mass flow choke rather than a traditional aerodynamic choke. Although around a set point of 40.5, the pressure ratios in the strut gap region appear to approach the pressure ratio indicating an aerodynamic choke, the consistent value of the secondary mass was significantly less than the theoretical value for an aerodynamic choke.

Ratios of secondary to primary mass flow rate were investigated as a function of primary to secondary flow total pressure ratio. The largest mass flow augmentation occurred at the lowest primary total pressure set point. As primary total pressure increased, both primary and secondary mass flow increased until the secondary mass flow choked. Primary mass flow continued to increase with increasing set point pressure, while secondary mass flow remained constant after the choking point. This caused the mass flow ratio to decrease linearly.

The duct pressure mixing distribution exhibited two distinct trends: a “low pressure” trend and a “high pressure” trend. For the low-pressure trend, the mixing length for the ejector occurred at approximately the same location along the mixing duct, regardless of the chamber pressure. For the high pressure trend, the mixing length was considerably longer and increased with increasing chamber pressure. At high chamber pressures (high mass flow rates), a supersonic core flow was observed at the exit of the duct. Mixing duct exit Mach numbers were determined and found to reach a sonic exit core flow for set points above 50.3. In general, the exit Mach numbers were less than expected, and may be attributed to the enhanced mixing and 3-D effects of the asymmetric geometry, or losses in the long the mixing duct.

The density-based CFD method was a useful tool to numerically simulate choking phenomena and stream mixing. The impact of various turbulence models was evaluated using 2-D calculations with exact ejector exit boundary conditions obtained from 3-D ejector-nozzle computations. In the flow regions dominated by stream mixing, compressibility correction was found to be necessary to capture the decreased spreading rate of compressible flow streams. Simulations using the Baldwin-Lomax and the SST two-equation models adequately predicted the measured quasi-2D sidewall pressures profiles. The compressibility-corrected k-ε model predicted the mixing pattern correctly in both 2-D (side-wall data comparison) and 3-D (top wall data comparison) simulations. However, the wall functions used in the k-ε model, even with compressibility correction, cannot reproduce wall-dominated phenomena, such as pressure recovery. Full 3-D modeling with wall-resolving turbulence models is required to capture the complex strut-base separation features. Full 3-D parallel computations, incorporating a compressibility corrected SST model will be the focus of future studies.

4. SUMMARY

This study of a non-axisymmetric strut-based ejector yielded several significant results. Measured strut gap and duct wall static pressure profiles showed that a mass flow choke occurs in the duct for all primary flow pressures rather than a traditional aerodynamic choke. The pressure distributions along the mixing duct wall showed a low primary pressure regime in which the mixing length location was essentially fixed. A high pressure regime was also identified with a considerably longer, pressure dependent mixing length. Comparisons between sidewall pressures profiles predicted by a RANS computational model and the quasi-2D experimental data indicate the Baldwin-Lomax and the SST two-equation models are capable of capturing essential flow features.

ACKNOWLEDGEMENTS

This work was supported by NASA Grant NCC8-200 with NASA MSFC with Mary Trawek as the COTR for NASA and the late Dr. Clark W. Hawk as Principal Investigator for the UAHuntsville Propulsion Research Center.

REFERENCES

[1] S.N.B. Murthy, and E.T. Curran, High Speed Flight Propulsion Systems, *Progress in Aeronautics and Astronautics*, 1991,Vol. 137, AIAA, Inc., Washington DC.

[2] M. Bulman and A. Siebenhaar, *The Strutjet Engine: Exploding the Myths Surrounding High Speed Airbreathing Propulsion*, AIAA Paper 1995, 2475.

[3] D. Landrum, M. Thames, D. Parkinson, and S. Gautney, *Investigations of the Rocket Induced Flow Field in a Rectangular Duct*, AIAA Paper 1999, 2100.

[4] D. Lineberry, N. Smith, D.B. Landrum, and C.W. Hawk, *Characterization of Cold Flow Non-Axisymmetric Ejectors*, AIAA Paper 2003, 5231.

[5] D. Lineberry, *Characterization of a Cold Flow Non-Axisymmetric Supersonic Ejector*, Dissertation, Dept. of Mechanical and Aerospace Engineering, UAHuntsville, 2007.

[6] H.W. Coleman, and W.G. Steele, *Experimentation and Uncertainty Analysis for Engineers*, Wiley-Interscience, 1999.

[7] ESI Corporation, *CFD* Fastran Theory Manual, 2003.

[8] D. Wilcox, *Turbulence Modeling for CFD*, DCW Industries Inc., Griffin Printing, CA, 1994.

[9] B.S. Baldwin, and H. Lomax, *Thin Layer Approximation and Algebraic Model for Separated Turbulent Flows*, AIAA Paper 1978, 0257.

[10] P.R. Spalart, and S.R. Allmaras, *A One equation Model for Aerodynamic Flows,* AIAA Paper 1992, 0439.

[11] B.E. Launder, and D.E. Spalding, D. E., The Numerical Computation of Turbulent Flow, *Comp. Methods App. Mech. Eng.*, 1974, 3, 269-289.

[12] F.R. Menter, *Zonal Two Equation Model for Aerodynamic Flows*, AIAA Paper 1993, 2906.

[13] F.R. Menter, F. R., Two Equation Eddy-viscosity Turbulence Models for Engineering Applications, *AIAA Journal*, 1994, 32, 1598-1606.

[14] P.L. Roe, Approximate Riemann Solvers, Parameter Vectors, and Difference Schemes, *Journal of Computational Physics,* 1981, 43(3), 57-372.

[15] S.J. Osher, and S. Chakravarthy, Upwind Schemes and Boundary Conditions with Applications to Euler Equations in General Geometries, *Journal of Computational Physics*, 1983, 50, 447-81.

[16] J. Fabri, and R. Siestrunck, Supersonic Air Ejectors, *Advances in Applied Mechanics*, Academic Press, NY, NY, 1958, 5, 1-34.

[17] J. Fabri, and J. Paulon, *Theory and Experiments on a Supersonic Air-To Air Ejectors*, NACA Technical Memorandum, 1956, 1410.

[18] K. Matsuo, Y. Miyazato, and H.D. Him, Shock Train and Pseudo-shock Phenomena in Internal Gas Flows, *Prog. In Aserospace Science*, 1999, 35, 33-100.

[19] Y. Bartosiewicz, Z. Aidoun, P. Desevaux, and Y. Mercadier, Numerical and Experimental Investigations on Supersonic Ejectors," *Int. J. Heat and Fluid Flow*, 2005, 26, 56-70.

[20] O. Zeman, Dilatational Dissipation: The Concept and Application in Modeling Compressible Mixing Layer, *Physics of Fluids A*, 1990, 2(2), 178-188.

[21] J.R. Viegas, and M.W. Rubesin, *A Comparative Study of Several Compressibility Corrections to Turbulence Models Applied to High Speed Shear Layers*, AIAA Paper 1991, 1783.

[22] S. Sarkar, G. Erlebacher, M.Y. Hussaini, and H.O. Kreiss, The Analysis and Modeling of Dilatational Terms in Compressible Turbulence, *J. Fluid Mech.*, 1991, 227, 473-493.

[23] J.R. Forsythe, K.A. Hoffmann, and Y.B. Suzen, *Investigation of Modified Menter's Two-Equation Turbulence Models for Supersonic Applications*, AIAA Paper 1999, 0873.